ACS NANO

www.acsnano.org

ARTICLE

Using the High-Entropy Approach to Obtain Multimetal Oxide Nanozymes: Library Synthesis, *In Silico* Structure–Activity, and Immunoassay Performance

Thuong Phan-Xuan,[††] Simon Schweidler,[††] Steffen Hirte,[††] Moritz Schüller, Ling Lin, Anurag Khandelwal, Kai Wang, Jan Schützke, Markus Reischl, Christian Kübel, Horst Hahn, Gianluca Bello, Johannes Kirchmair, Jasmin Aghassi-Hagmann, Torsten Brezesinski, Ben Breitung,* and Lea Ann Dailey*

Cite This: *ACS Nano* 2024, 18, 19024–19037

Read Online

ACCESS | Metrics & More | Article Recommendations | Supporting Information

ABSTRACT: **High-entropy nanomaterials exhibit exceptional mechanical, physical, and chemical properties, finding applications in many industries. Peroxidases are metalloenzymes that accelerate the decomposition of hydrogen peroxide. This study uses the high-entropy approach to generate multimetal oxide-based nanozymes with peroxidase-like activity and explores their application as sensors in *ex vivo* bioassays. A library of 81 materials was produced using a coprecipitation method for rapid synthesis of up to 100 variants in a single plate. The A and B sites of the magnetite structure, $(AA')(BB'B'')_2O_4$, were substituted with up to six different cations (Cu/Fe/Zn/Mg/Mn/Cr). Increasing the compositional complexity improved the catalytic performance; however, substitutions of single elements also caused drastic reductions in the peroxidase-like activity. A generalized linear model was developed describing the relationship between material composition and catalytic activity. Binary interactions between elements that acted synergistically or antagonistically were identified, and a single parameter, the mean interaction effect, was observed to correlate highly with catalytic activity, providing a valuable tool for the design of high-entropy-inspired nanozymes.**

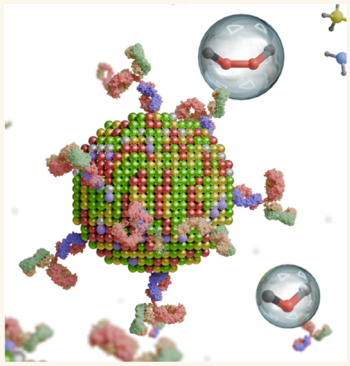

KEYWORDS: *high-entropy oxides, spinels, peroxidase, ELISA, high-throughput, generalized linear model, antibody*

INTRODUCTION

Nanozymes are inorganic nanomaterials with intrinsic enzyme-like catalytic activity, i.e., the ability to catalyze chemical reactions under physiological conditions. Metal, metal-oxide/metal-sulfide, and carbon-based nanozymes[1] have found numerous applications in redox-based and photocatalytic applications.[2−4] In 2007, Gao et al. reported that pure magnetite (inverse spinel, Fe_3O_4) nanoparticles can trigger the decomposition of hydrogen peroxide (H_2O_2) at a rate comparable to that of horseradish peroxidase.[5] In human metabolism, peroxidases are metalloenzymes that accelerate the decomposition of hydrogen peroxide (H_2O_2) in order to prevent cell damage. The catalytically active center in horseradish peroxidase (HRP) is a heme-bound Fe(III) ion, which is postulated to oxidize to Fe(IV) and cycle back to Fe(III) during the catalytic process, although the exact mechanism is still unknown.[6] The catalytic activity reported for magnetite was quite surprising since until that point magnetite had been considered an inert material. A debate focusing on the extent of magnetite-mediated catalysis emerged.[7−9] Although the definitive verdict of whether magnetite nanoparticles are truly "catalytically active" still remains unclear, applications employing magnetite nanozymes have been reported.[10,11] Nonetheless, Lu et al. showed that in a direct comparison of Fe_3O_4 to DNAzymes and HRP, the stability of Fe_3O_4 nanozymes is higher under a variety of conditions, even if the turnover rate is lower compared to the native enzyme.[12] In addition to Fe_3O_4, other nanozyme classes

Received: March 6, 2024
Revised: May 14, 2024
Accepted: May 23, 2024
Published: July 10, 2024

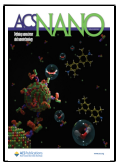

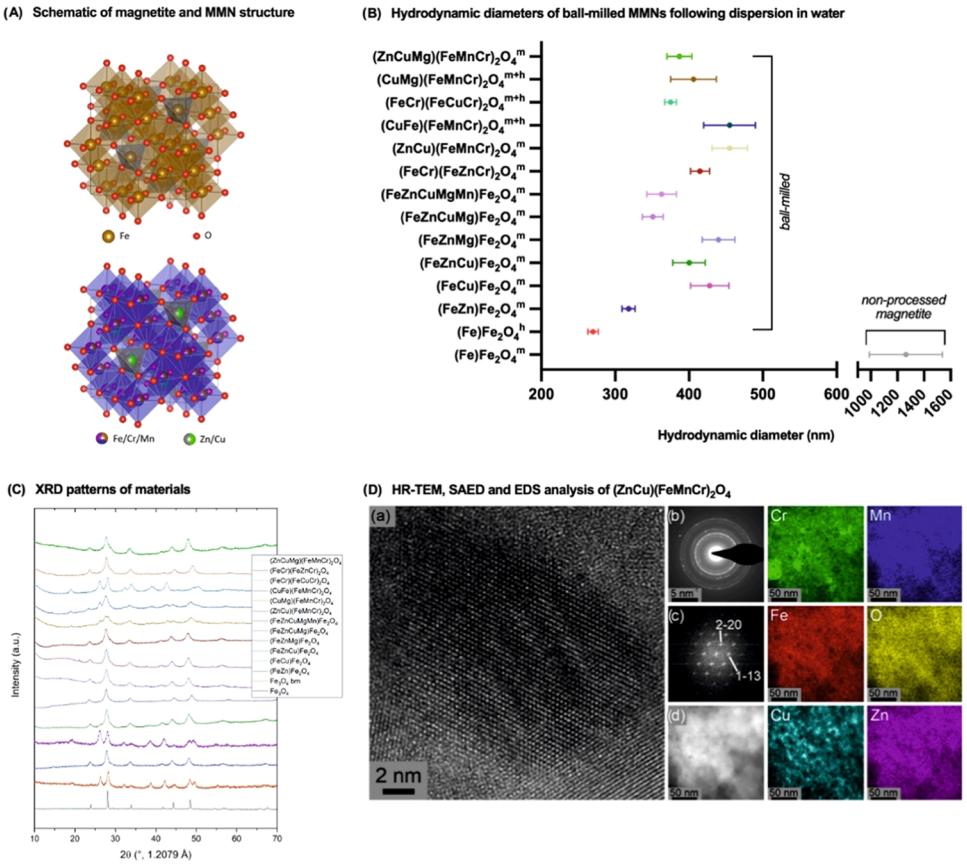

Figure 1. (A) Inverse spinel structure of (Fe)Fe_2O_4 and the spinel structure of a representative MMN: (ZnCu)$(FeMnCr)_2O_4$, (B) hydrodynamic diameters of MMNs produced by ball-milling and measured by DLS (superscripts: m = magnetite, h = hematite, and m+h = magnetite/hematite), (C) X-ray diffraction (XRD) patterns of nonprocessed (Fe)Fe_2O_4 and ball-milled materials, and (D) high-resolution transmission electron microscopy (HR-TEM) micrograph of (ZnCu)$(FeMnCr)_2O_4$: (a) selected area electron diffraction (SAED) of the (ZnCu)$(FeMnCr)_2O_4$, indicating a single-phase spinel structure, (b) Fourier transform (FFT) of the crystallite, (c) high-angle annular dark-field scanning transmission electron microscopy (HAADF-STEM) micrograph, and (d) energy-dispersive spectrometry (EDS) images of (ZnCu)$(FeMnCr)_2O_4$ showing the elemental distribution in projection.

have been developed. Improvements in the catalytic activity have been achieved by simulating the microenvironment of natural enzymes,[13] incorporating more active species,[14,15] and designing single-atom catalysts[16,17] and surface modification.[18] The investigation of bimetallic nanoparticles (e.g., $CoFe_2O_4$[19] or MFe_2O_4, whereby M = Mg, Ni, Zn[20]) has led to nanozymes with enhanced peroxidase-like activity and tunable enzymatic-like properties. Luo et al. reported that trimetallic nanozymes composed of $Co_xNi_{1-x}Fe_2O_4$ can also be used as sensors to detect H_2O_2.[21]

In 2015, Rost et al. described the preparation of the rock salt-structured high-entropy (CoCuMgNiZn)O. Materials that incorporate many different cations in near equimolar ratios into a single-phase structure are now known as high-entropy materials (HEMs).[22] What makes these compounds special is the effects of introducing many different elements into a lattice. This can result in lattice distortions, cocktail effects, and a high configurational entropy, all of which can influence the material properties. The elemental interactions vary with composition and stoichiometry and therefore allow tailoring of material properties by changing these conditions.[23] The classification of HEMs is purely empirical, whereby materials with a configurational entropy (S_{config}) above 1.5R (Equation; Figure S1) are called "high-entropy" materials, while materials below this threshold are described as "medium-entropy" or "low-entropy" materials. Diverse ceramic high-entropy classes, including oxides, nitrides, carbides, sulfides, fluorides, phosphates, and carbonitrides, have been described in the literature, and they exhibit a variety of structures (e.g., spinel, rock salt, fluorite, perovskite, *etc.*).[24] HEMs have been shown to exhibit exceptional mechanical, physical (e.g., electrical and magnetic), and chemical (e.g., catalytic) properties, finding applications in the aerospace industry,[25−27] electronics, optoelectronics, photovoltaic, and thermoelectric devices,[28,29] as well as battery technologies and fuel cells,[30−32] low-cost electrolysis of water,[33,34] and carbon capture strategies.[35] However, to date, there have been few investigations into the biomedical applications of HEMs,[36−38] including their use as multimetal-based nanozymes (MMNs).[39]

RESULTS

HEM-Inspired MMNs Produced via High-Energy Planetary Ball-Milling. Precursor materials (pure metal oxides) were mixed in the desired stoichiometric ratios and ball-milled under an argon atmosphere to obtain cubic and trigonal materials with a $(AA')(BB'B'')_2O_4$ structure. Starting from magnetite $(Fe(II)Fe(III)_2O_4)$, Fe(II) in the AA' position was replaced with the divalent cations Zn, Cu, Mg, or Mn. The Fe(III) in the BB'B'' position was replaced with the trivalent ions, Mn and Cr. The stoichiometry of the elements is always

https://doi.org/10.1021/acsnano.4c03053
ACS Nano 2024, 18, 19024−19037

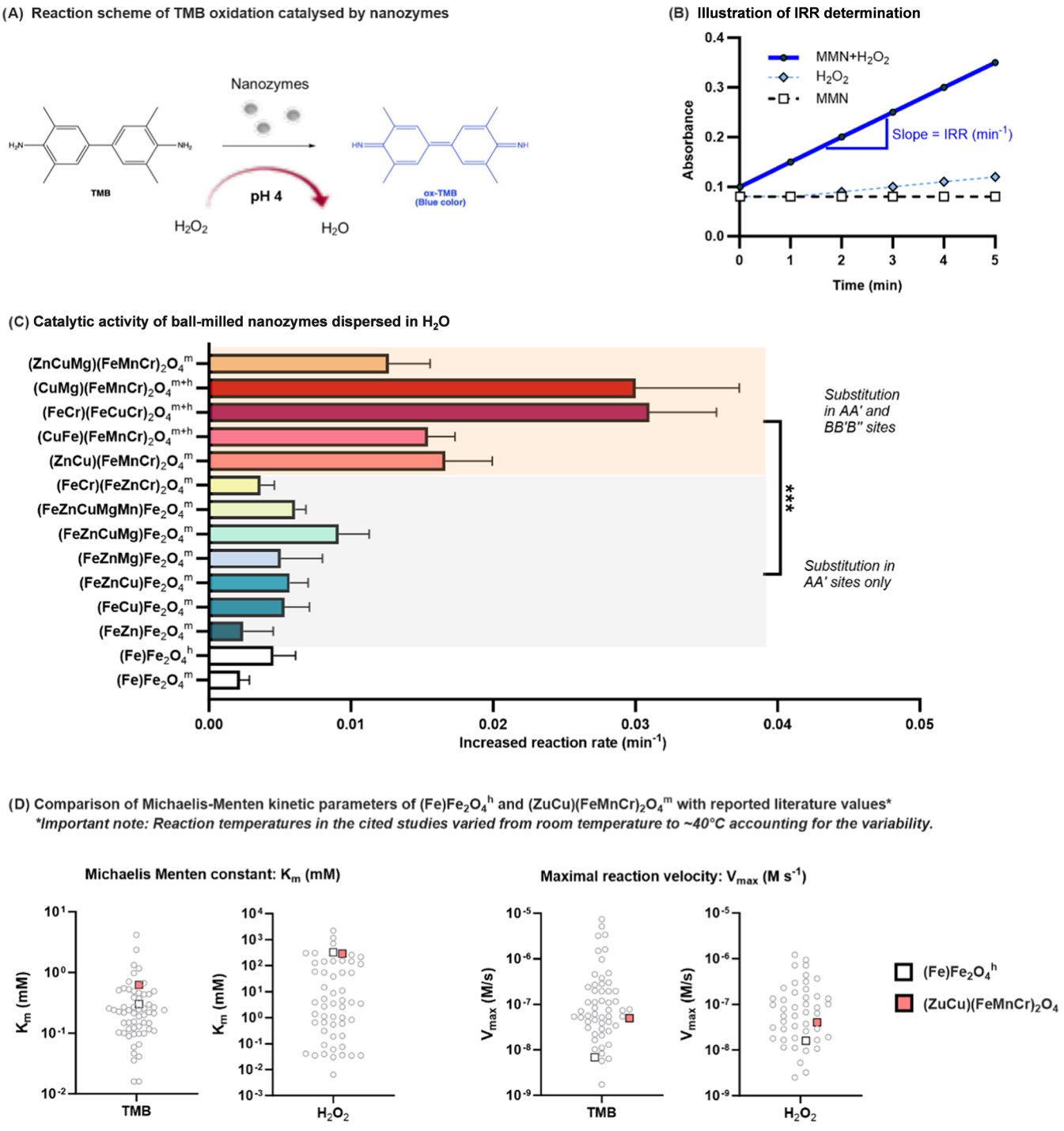

Figure 2. (A) TMB oxidation by H_2O_2 is accelerated in the presence of nanozymes, (B) Illustration of how the IRR (min^{-1}) value is determined from the ox-TMB absorbance profile, and (C) IRR (min^{-1}) of nonprocessed $(Fe)Fe_2O_4$ and ball-milled nanozymes dispersed in water (mean ± standard deviation; n = 12). All dispersions were prepared from a single production batch. ***p < 0.001. Superscripts: ^{m}magnetite, ^{h}hematite, and $^{m+h}$magnetite+hematite. (D) Comparison of the Michaelis−Menten parameters, K_m (mM) and V_{max} (M/s), with literature values summarized by Zhang et al.[45] It is important to note that the reaction temperature of the cited studies varied from ambient room temperature to ~40 °C, which accounts for the high variation in the cited parameters.

equimolar; therefore, the composition of $(FeCu)Fe_2O_4$ can also be written as $Fe_{0.5}Cu_{0.5}Fe_2O_4$. In a subset of materials, such as $(FeCr)(FeCuCr)_2O_4$, we also attempted to incorporate partially trivalent ions into the A site and divalent ions into the B site, as this switch is also possible in inverse spinels (note: the oxygen content might vary accordingly). Figure 1A shows a schematic of a magnetite inverse spinel and a high-entropy spinel (e.g., $(ZnCu)(FeCrMn)_2O_4$), whereby Zn(II) and Cu(II) replace Fe(II) and a mixture of Fe(III), and Cr(III) and Mn(III) replace Fe(III) in $(Fe)Fe_2O_4$.

Hydrodynamic diameters of ball-milled materials were measured using dynamic light scattering (DLS) and ranged from 250 to 400 nm (Figure 1B; Figure S1). The non-processed $Fe(Fe)_2O_4$ was substantially larger (~1200 nm).

https://doi.org/10.1021/acsnano.4c03053
ACS Nano 2024, 18, 19024−19037

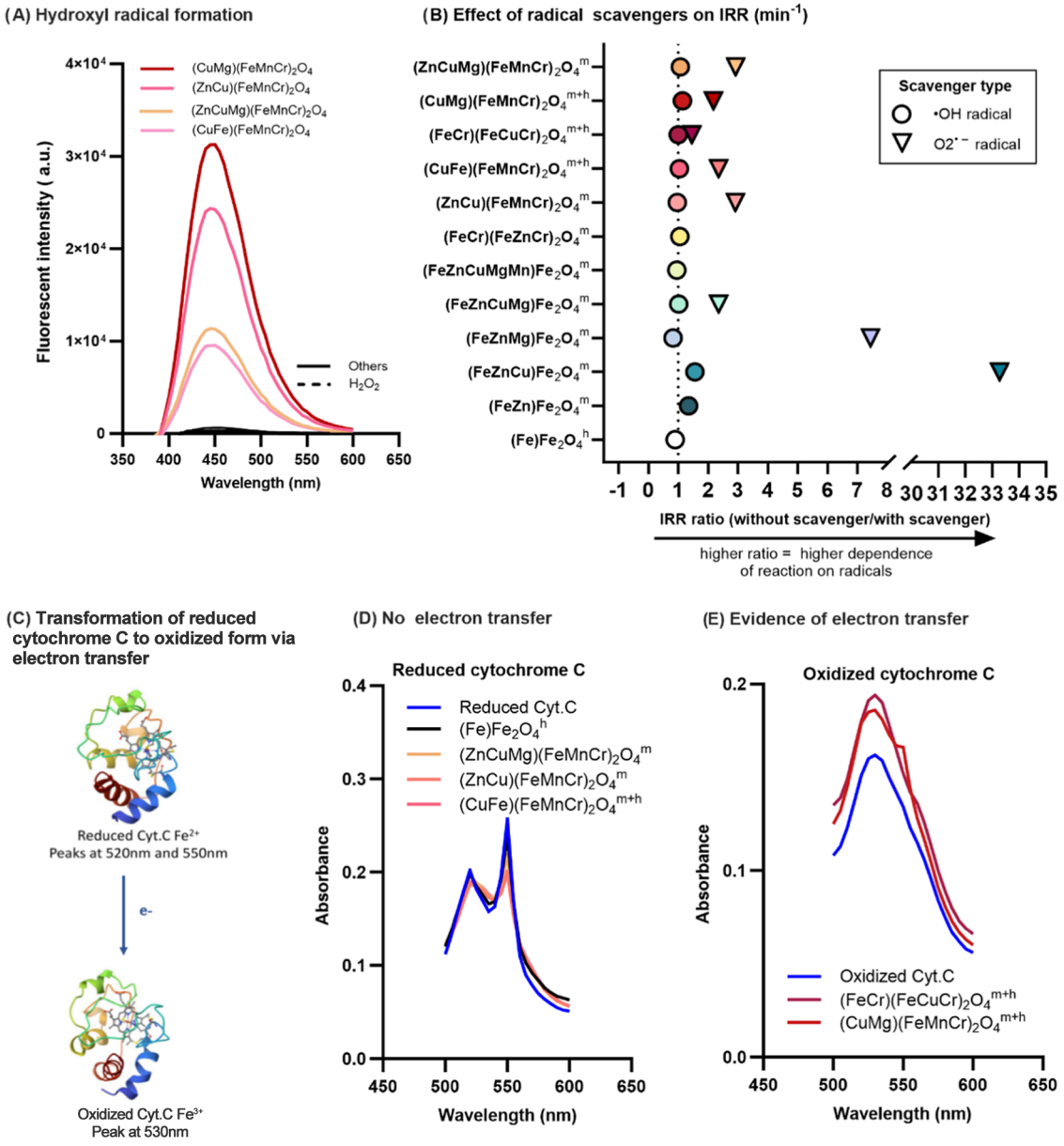

Figure 3. (A) Hydroxyl radical formation detected using terephthalic acid fluorescence emission as a quantitative measure of radical generation (n = 3). (B) Influence of radical scavengers on the reaction rate expressed as the ratio of the mean IRR without scavenger: mean IRR with scavenger (n = 3). Values >1 indicate that the radical plays a mechanistic role in the reaction. (C) Illustration of the transformation from reduced cytochrome C to oxidized cytochrome C via electron donation. (D) Absorbance spectra of reduced cytochrome C alone (blue line) and in the presence of ball-milled materials that do not exhibit electron transfer (others). (E) Absorbance spectra of oxidized cytochrome C alone (blue line) and in the presence of two materials exhibiting electron-transfer properties (others).

The MMN crystal structure and phase purity were assessed using X-ray diffraction (XRD; Figure 1C) and Rietveld analysis (Figure S2). Interestingly, the harsh ball-milling conditions changed the $(Fe)Fe_2O_4$ magnetite structure to a hematite structure after a short milling time. The same conversion was also observed with $(FeCu)Fe_2O_4$, while most of the other materials showed a spinel structure after the ball-milling procedure. Exceptions are materials $(CuMg)(FeMnCr)_2O_4$, $(CuFe)(FeMnCr)_2O_4$, and $(FeCr)(FeCuCr)_2O_4$, where a mixture of magnetite and hematite was observed (Figure 1C). Comparing the XRD pattern of $(ZnCu)(FeMnCr)_2O_4$ with that of the nonprocessed magnetite, reference material revealed that the reflections of the MMN are much broader compared to $(Fe)Fe_2O_4$, indicating smaller, defective crystallites resulting from the ball-milling process (Figure S2). A slight shift of the reflections to smaller angles is observed, indicating an increase in the lattice parameters and therefore a larger unit cell. This observation aligns with the larger ionic radii of the incorporated ions compared to $(Fe)Fe_2O_4$.[40] High-resolution transmission electron microscopy (HR-TEM) investigations were conducted for two materials, $(ZnCu)(FeMnCr)_2O_4$ (Figure 1D) and $(ZnCuMg)(FeMnCr)_2O_4$ (Figure S3), revealing a high crystallinity as seen in the observable lattice planes (Figure 1Da; Figure S3). The observed crystallite size matches the calculated size from XRD Rietveld refinement (Figure S2). The selected area diffraction (SAED, Figure 1Db) confirms these findings and clearly indicates a single-phase spinel structure of high

https://doi.org/10.1021/acsnano.4c03053
ACS Nano 2024, 18, 19024−19037

crystallinity for $(ZnCu)(FeMnCr)_2O_4$. Figure 1Dc also displays a fast Fourier transform (FFT) of the HR-TEM image in Figure 1Da, where the *d*-values correspond to 2.97 and 2.53 Å for the lattice planes of a spinel structure (*hkl* indices: 2−20 and 1−13, respectively; in the [110] zone axis orientation). Energy-dispersive X-ray spectroscopy (EDS) provided information about the spatial elemental distribution in the $(ZnCu)(FeMnCr)_2O_4$ sample. The measurements reveal the distribution of individual elements on the nanometer scale, where an increase in color intensity indicates a higher concentration of the respective element, in this case Cu and Cr, indicating an inhomogeneous distribution.

Substitutions in Both Tetrahedral (AA′) and Octahedral (BB′B″) Sites of MMNs Generally Results in Higher Peroxidase-Like Activity. By introducing different elements homogeneously dispersed within a lattice, interactions between the elements can occur, which change the material properties.[30] More importantly, a very unique surface is formed with atomically distributed elements in very close proximity to each other, where each individual element acts as a catalytic center. This results in different chemical environments, which can serve as catalytically active centers.[41] The peroxidase-like activity of the ball-milled MMNs was assessed in three media to determine the baseline activity in water and evaluate whether common buffer solutions (phosphate-buffered saline, PBS, and tris(hydroxymethyl) aminomethane, TRIS pH 7.4) act as capping agents,[42−44] thus reducing peroxidase-like activity. Prior to analysis, all systems were washed once with buffer and redispersed in fresh medium, a step that significantly reduced experimental variability (Figure S4). The peroxidase-like activity was determined by measuring the reaction rate of tetramethylbenzidine (TMB) oxidation (Figure 2A; Figure S4). Since the presence of nanozymes accelerated the reaction rate compared to the baseline (H_2O_2 only), the increase in reaction rate (IRR; min^{-1}) above the peroxide control was used to express peroxidase-like activity (Figure 2B).

MMNs with elemental substitutions in both tetrahedral (AA′) and octahedral (BB′B″) sites exhibited significantly higher peroxidase-like activity compared to reference (Fe)-Fe_2O_4 nanozymes (magnetite and hematite) and MMNs with substitutions in the tetrahedral (AA′) site only (Figure 2C). The material $(FeCr)(FeZnCr)_2O_4$, was a notable exception to this trend, showing a very low peroxidase activity. Hypotheses as to why some materials with minor changes to elemental composition perform worse than others are discussed in further detail in the Supporting Information (SI). It is well-known that the incorporation of 3d transition metals into tetrahedral and octahedral sites of the spinel structure results in a significant effect on the catalytic activity toward H_2O_2.[46−48] A further important observation was that copper ions were present in all materials with enhanced peroxidase-like activity.

Two materials, ball-milled $(Fe)(Fe)_2O_4{}^h$ and $(ZnCu)$-$(FeMnCr)_2O_4{}^m$, were chosen for in-depth analysis of Michaelis−Menten kinetics to enable comparisons of performance with other iron oxide-based nanozymes reported in the literature (Figure 2D; Figure S8).[20,49−51] The Michaelis−Menten constant (K_m) and the maximum reaction velocity (V_{max}) were chosen as representative kinetic parameters for this comparison since these are the most commonly reported values in peroxidase-like nanozyme studies. The literature values reported were taken from a review by Zhang et al.[45] A small K_m indicates a higher affinity for the substrate, while a high V_{max} denotes a more rapid reaction rate. The summary in Figure 2D highlights that the reported K_m and V_{max} values (determined for both TMB and H_2O_2 as substrates) vary considerably in magnitude across the literature (Figure 2D). This variation likely results from the wide range of reaction temperatures employed in different studies (e.g., ambient room temperature to 40 °C).[5,52−54] Since K_m and V_{max} can be dramatically affected by reaction temperature, the variation is not unexpected. The K_m and V_{max} values calculated for the ball-milled $(Fe)(Fe)_2O_4{}^h$ and $(ZnCu)(FeMnCr)_2O_4{}^m$ in this study align with reported values in the literature, albeit in the lower affinity/velocity range. However, since all reactions performed in this study were conducted at ambient room temperature (22−25 °C), the results make sense within this context.

Involvement of Reactive Radicals and Electron-Transfer Process in Peroxidase-Like Activity of MMNs. It has been reported that reactive oxygen species, such as hydroxyl radicals ($^{\bullet}OH$) and superoxide radicals ($O_2^{\bullet-}$), are involved in the oxidation of TMB substrate of peroxidase-like activity displaying nanozymes.[55−57] To identify the impact of generated active species on the reaction rate, terephthalic acid and *p*-benzoquinone were used as scavengers of the $^{\bullet}OH$ and $O_2^{\bullet-}$ radicals, respectively. Terephthalic acid reacts with $^{\bullet}OH$ to produce a highly fluorescent derivative. As can be seen, nearly all MMNs with high catalytic activity also generated significant amounts of hydroxyl radicals (Figure 3A), with the exception of $(FeCr)(FeCuCr)_2O_4$, which exhibited one of the highest IRR values, but had a 51-fold lower hydroxyl radical generation (expressed as area under the fluorescence curve) than the most active MMN, $(CuMg)(FeMnCr)_2O_4$, indicating that $^{\bullet}OH$ radicals might not be responsible for TMB oxidation. Indeed, further experiments using radical scavengers confirmed that the IRR (min^{-1}) was not reduced in the presence of the hydroxyl radical scavenger, terephthalic acid (Figure 3B; circles), indicating that hydroxyl radical intermediates did not play a major role in the catalytic activity of nearly all materials tested. In contrast, the presence of the superoxide radical scavenger, *p*-benzoquinone, did show a substantial decrease in IRR (min^{-1}) for many of the ball-milled materials, implying a significant role of $O_2^{\bullet-}$ radicals in TMB oxidation (Figure 3B).

In the two most catalytically active materials, the peroxidase-like activity may also be attributed to electron-transfer processes. Electron transfer is typically measured using the reduced form of cytochrome C as a marker since oxidation via electron-transfer results in a dramatic shift in the absorbance spectrum (Figure 3C). Cytochrome C remained in the reduced form in the presence of four selected ball-milled MMNs (Figure 3D), indicating that no electron transfer occurred. In the presence of $(FeCr)(FeCuMn)_2O_4$ and $(CuMg)$-$(FeMnCr)_2O_4$, the oxidized form of cytochrome C was detected (Figure 3E), indicating that these materials likely act as an electron mediator between TMB and H_2O_2, a mechanism which has also been reported in other studies.[58,59] For example, Warkhade et al. postulated that the large potential band gap between TMB (1.12 V) and H_2O_2 (1.566 V) makes it difficult for electrons to be transferred directly between the two molecules. They observed that the reduction potential of $CoSe_2$ nanoflakes (1.2 V) was in between that of TMB and H_2O_2, thus facilitating electron transfer and TMB oxidation.[58] A similar observation was found in Ce-doped $ZnCo_2O_4$ nanoparticles, whereby the enhanced peroxidase-like activity was attributed to a co-contribution of superoxide radicals and electron transfer.[60]

https://doi.org/10.1021/acsnano.4c03053
ACS Nano 2024, 18, 19024−19037

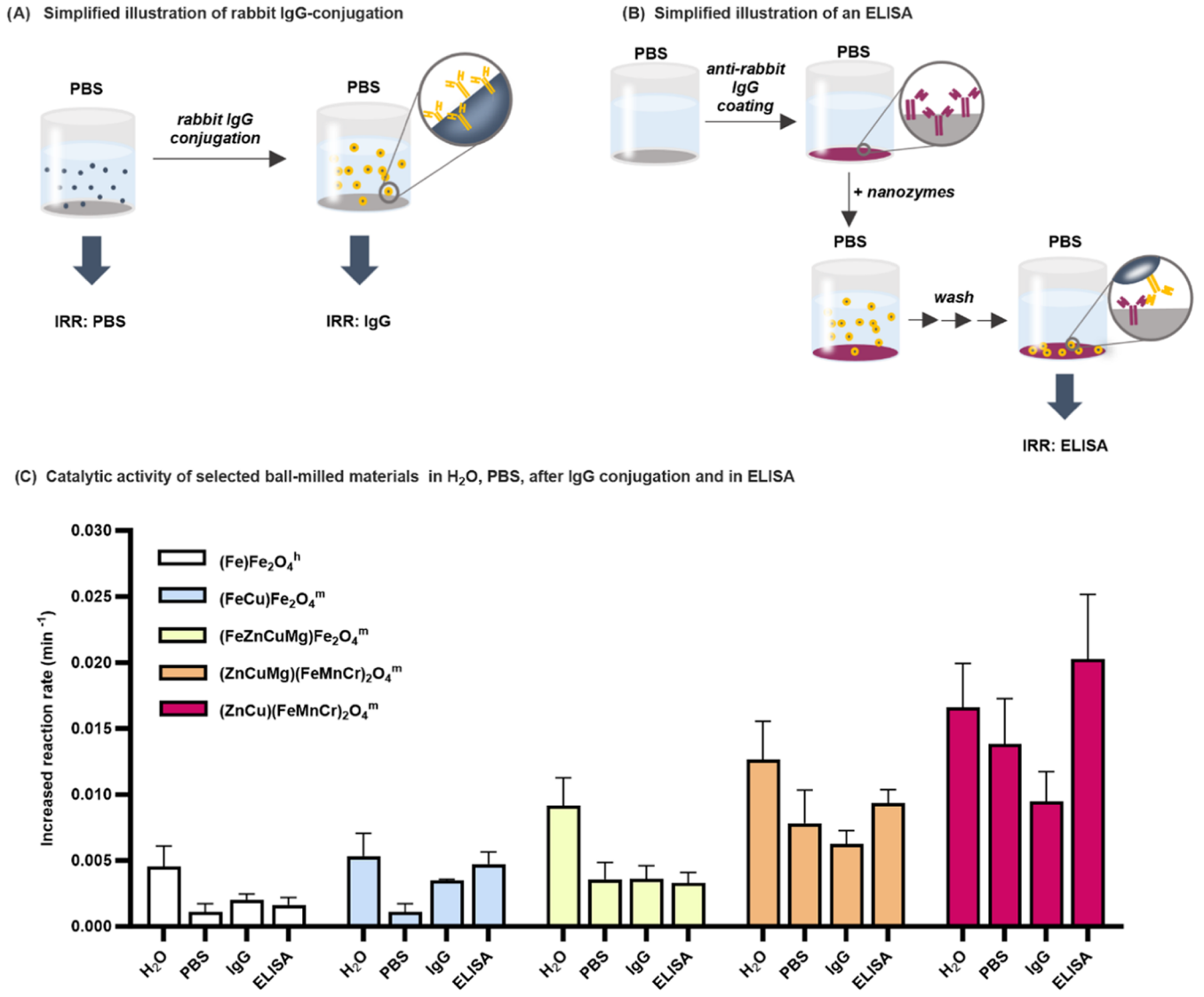

Figure 4. Feasibility studies demonstrating MMN performance in an *ex vivo* ELISA application. Simplified illustration of the IgG conjugation process (A) and ELISA (B). The catalytic activities of five selected ball-milled material in water (n = 12), in PBS (N = 12), after IgG conjugation (n = 4), and in the ELISA (n = 3). Results are portrayed as the mean ± standard deviation, and all dispersions were prepared from a single ball-milled production batch.

Effect of Surface Modification on Peroxidase-Like Activity and *Ex Vivo* Bioassay Feasibility Assessment. Nanozymes may be used as an alternative to horseradish peroxidase in *ex vivo* enzyme-linked immunosorbent assays (ELISA). Compared to natural enzyme labels, which can suffer from low stability, high production costs, and the need for refrigerated storage, nanozymes are associated with tunable catalytic activities, easy preparation, low costs, and high stability, even under extreme storage conditions.[61] To assess MMN activity in an ELISA application, rabbit immunoglobulin G (IgG) antibodies were conjugated to the surface of five ball-milled materials by using a conventional antibody modification protocol (Figure 4A). Buffers such as PBS and TRIS are commonly employed in antibody conjugation reactions; thus, their effect on catalytic activity was assessed. Surface capping by PBS and TRIS led to reduced catalytic activity in most MMNs compared to dispersions in water (Figure 4C; Figure S6).[62] Distinct trends were, however, not observed, and PBS was used in further experiments. Surface modification with rabbit IgG antibodies showed no discernible trends when compared to the activity of nonmodified materials in PBS (Figure 4C). When employed in a simplified ELISA assay (schematic in Figure 4B), the catalytic activity was either similar or higher than that of the dispersed IgG-conjugated materials, indicating (1) that the IgG conjugation to the nanozyme surface was successful, (2) the conjugation process did not negatively impact rabbit IgG binding to its antirabbit IgG counterpart, and (3) nanozyme activity was preserved in the ELISA.

Exploring the Cocktail Effect on MMN Catalytic Activity Using Coprecipitation Synthesis. To better understand why such large differences in catalytic activity were observed in MMNs with substitutions in both the tetrahedral and octahedral sites (Figure 2C), a larger data set was required. Preparation via ball-milling is time-consuming, thereby limiting the number of materials produced within a reasonable period. For this reason, different MMN variants were prepared using a coprecipitation approach (>100 samples

https://doi.org/10.1021/acsnano.4c03053
ACS Nano 2024, 18, 19024−19037

Table 1. Structures of Coprecipitated MMNs Including Their Ranking According to Catalytic Activity[a]

R	material	R	material	R	material
15	$(FeCr)(FeCuCr)_2O_4^{a}$*	56	$(CrMn)(FeMnZn)_2O_4^{m}$	47	$(MnZn)(CrFeMg)_2O_4^{m+x}$
28	$(ZnCu)(FeMnCr)_2O_4^{m+h}$*	42	$(CrMn)(FeMnMg)_2O_4^{m+h}$	51	$(MnZn)(CrFeFe)_2O_4^{m+h}$
19	$(CuMg)(FeMnCr)_2O_4^{m}$*	60	$(CrMn)(FeMnFe)_2O_4^{m+h}$	4	$(MnZn)(CrFeCu)_2O_4^{m+x}$
29	$(ZnMg)(FeMnCr)_2O_4^{m}$	23	$(CrMn)(FeMnCu)_2O_4^{m}$	30	$(MnZn)(CrFeMn)_2O_4^{m}$
39	$(ZnFe)(FeMnCr)_2O_4^{m}$	32	$(FeZn)(CrMnMg)_2O_4^{a}$	6	$(MnCu)(CrFeZn)_2O_4^{m}$
33	$(ZnMn)(FeMnCr)_2O_4^{a}$	62	$(FeZn)(CrMnFe)_2O_4^{m+h}$	9	$(MnCu)(CrFeMg)_2O_4^{m+h}$
55	$(MgFe)(FeMnCr)_2O_4^{m}$	5	$(FeZn)(CrMnCu)_2O_4^{m}$	14	$(MnCu)(CrFeFe)_2O_4^{m+h}$
26	$(MgMn)(FeMnCr)_2O_4^{m}$	36	$(FeZn)(CrMnMn)_2O_4^{m}$	10	$(MnCu)(CrFeMn)_2O_4^{m}$
31	$(FeMn)(FeMnCr)_2O_4^{m+h+x}$	13	$(FeCu)(CrMnZn)_2O_4^{m}$	63	$(MnMg)(CrFeZn)_2O_4^{m}$
2	$(CuMn)(FeMnCr)_2O_4^{a}$	1	$(FeCu)(CrMnMg)_2O_4^{a}$	65	$(MnMg)(CrFeFe)_2O_4^{m+h}$
35	$(CrZn)(FeMnMg)_2O_4^{m}$	11	$(FeCu)(CrMnFe)_2O_4^{a}$	25	$(MnMg)(CrFeCu)_2O_4^{m}$
53	$(CrZn)(FeMnFe)_2O_4^{m+h}$	3	$(FeCu)(CrMnMn)_2O_4^{m+h}$	43	$(MnMg)(CrFeMn)_2O_4^{m+h}$
7	$(CrZn)(FeMnCu)_2O_4^{m+x}$	41	$(FeMg)(CrMnZn)_2O_4^{m}$	70	$(MnFe)(CrFeZn)_2O_4^{m+h}$
34	$(CrZn)(FeMnMn)_2O_4^{m}$	69	$(FeMg)(CrMnFe)_2O_4^{m+h}$	45	$(MnFe)(CrFeMg)_2O_4^{m+h}$
17	$(CrCu)(FeMnZn)_2O_4^{m+x}$	16	$(FeMg)(CrMnCu)_2O_4^{m}$	24	$(MnFe)(CrFeCu)_2O_4^{m+h}$
8	$(CrCu)(FeMnMg)_2O_4^{m}$	38	$(FeMg)(CrMnMn)_2O_4^{m}$	54	$(MnFe)(CrFeMn)_2O_4^{m+h}$
21	$(CrCu)(FeMnFe)_2O_4^{m+h}$	64	$(FeFe)(CrMnZn)_2O_4^{m+h}$	49	$(MnMn)(CrFeZn)_2O_4^{m}$
12	$(CrCu)(FeMnMn)_2O_4^{m}$	57	$(FeFe)(CrMnMg)_2O_4^{a}$	46	$(MnMn)(CrFeMg)_2O_4^{m}$
44	$(CrMg)(FeMnZn)_2O_4^{m}$	27	$(FeFe)(CrMnCu)_2O_4^{m+h}$	40	$(MnMn)(CrFeFe)_2O_4^{m+h}$
61	$(CrMg)(FeMnFe)_2O_4^{a}$	58	$(FeFe)(CrMnMn)_2O_4^{a}$	18	$(MnMn)(CrFeCu)_2O_4^{m}$
22	$(CrMg)(FeMnCu)_2O_4^{a}$	50	$(FeMn)(CrMnZn)_2O_4^{m}$	*R = Ranking*	
37	$(CrMg)(FeMnMn)_2O_4^{a}$	66	$(FeMn)(CrMnMg)_2O_4^{m}$	^{a}amorphous	
68	$(CrFe)(FeMnZn)_2O_4^{m+h}$	67	$(FeMn)(CrMnFe)_2O_4^{m+h+x}$	^{m}magnetite	
59	$(CrFe)(FeMnMg)_2O_4^{m+h}$	20	$(FeMn)(CrMnCu)_2O_4^{m}$	$^{m+h}$magnetite+hematite	
48	$(CrFe)(FeMnCu)_2O_4^{m}$			^{x}unidentified phase	
52	$(CrFe)(FeMnMn)_2O_4^{m+h+x}$			*Match with ball-milled materials	

[a]R = Rank order from highest (1) to lowest (70) peroxidase-like activity. Phase properties are also indicated via the superscript: [a]amorphous, [m]magnetite, and [m+h]magnetite+hematite. An asterisk indicates materials that were also included in the ball-milled subset. Please note that the composition presented here, as well as the distribution of elements within the A and B sites, is solely based on the amount of precursors employed during the synthesis process. The actual distribution of elements on the A and B sites has not been determined, and as a result, the true chemical formula may deviate. However, it is worth mentioning that the majority of the materials investigated exhibit structures resembling either hematite or magnetite, without the presence of additional phases.

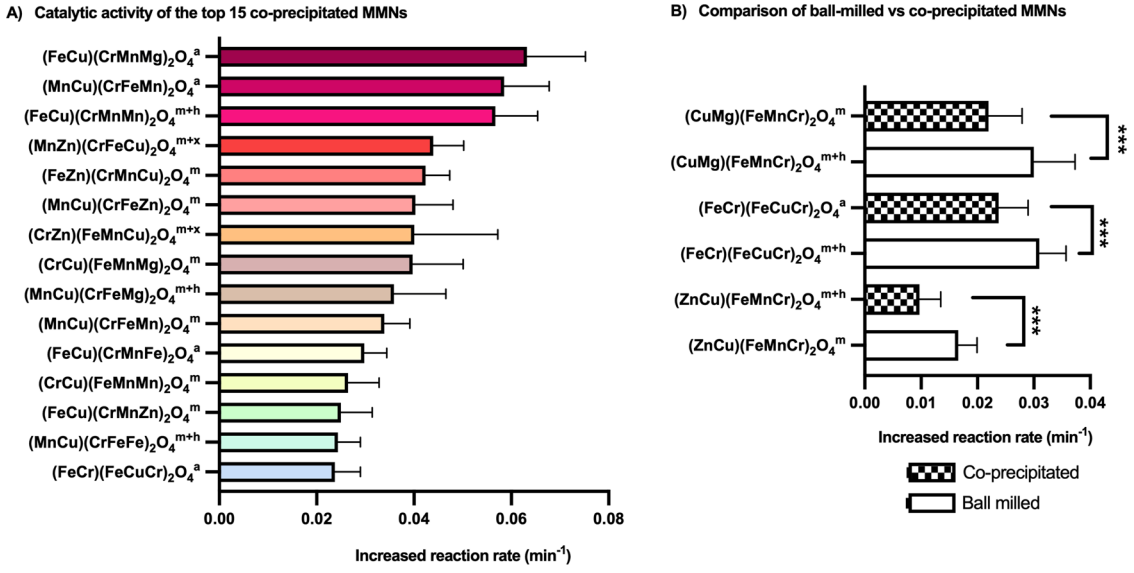

Figure 5. Peroxidase-like catalytic activity of coprecipitated MMNs. (A) IRR values of the 15 top-performing materials from the coprecipitated MMN subset, in order of decreasing catalytic activity from top to bottom (n = 12). (B) Comparison of the IRR values of three materials prepared both by ball milling and coprecipitation (n = 12). Dispersions were prepared from a single nanozyme production batch. ns = nonsignificant; ***p < 0.001.

in one batch). A subset of 70 distinct materials with elemental substitutions in both the AA' and BB'B'' sites was produced via coprecipitation (Table 1), including three materials with structures corresponding to their ball-milled counterparts. XRD analysis (Figure S9) revealed that 43% of the coprecipitated materials exhibited a magnetite structure,

https://doi.org/10.1021/acsnano.4c03053
ACS Nano 2024, 18, 19024−19037

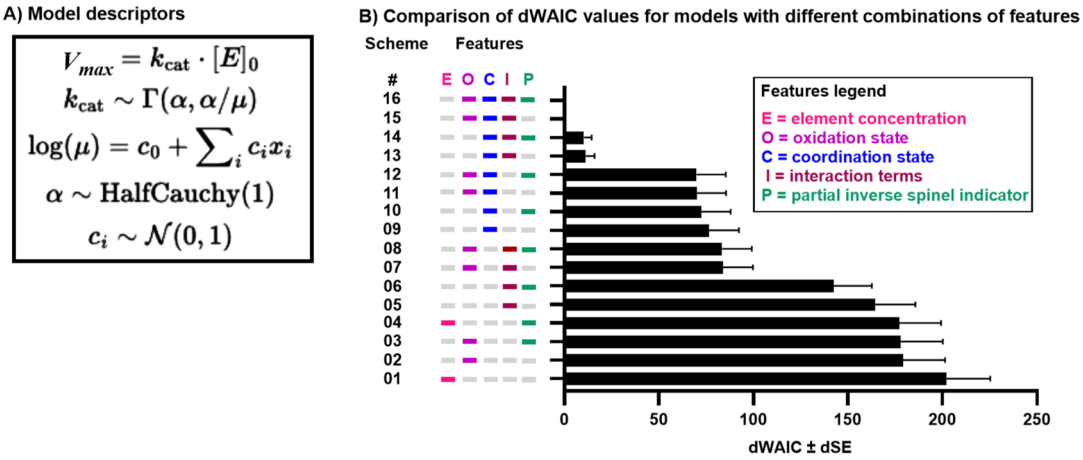

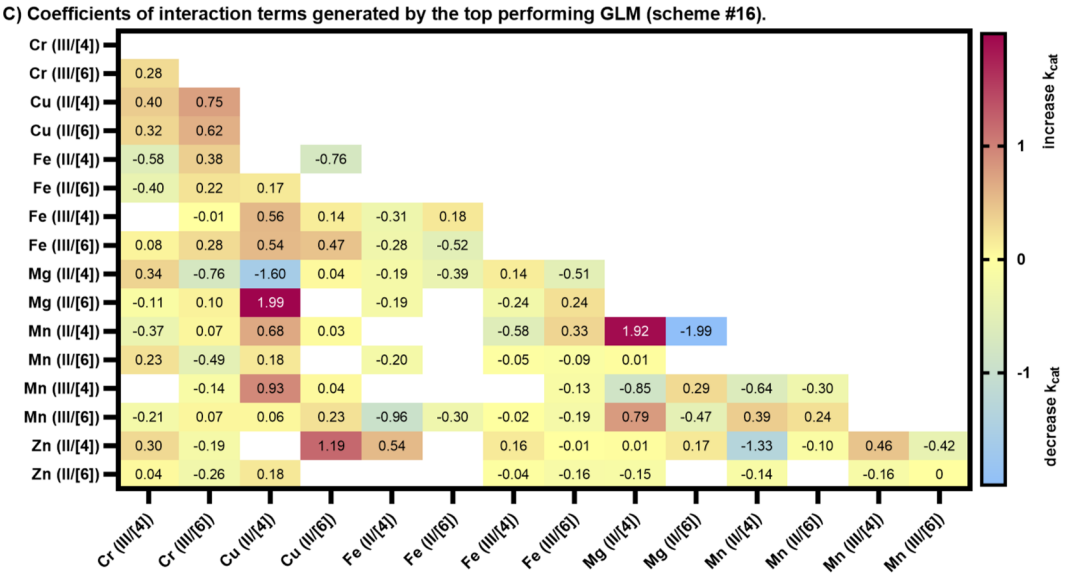

D) Example calculation of mean interaction effect (MIntE)

$$\textit{Mean interaction effect} = e^{\sum(c_{pair}\cdot[a]\cdot[b])}$$

c_{pair} = coefficient of interaction terms
a = molar concentration of partner a in the interaction pair
b = molar concentration of partner b in the interaction pair

#	Interaction pairs for $(MgMn)(CrFeMn)_2O_4$	c_{pair}	[a]	[b]	$c_{pair}\cdot[a]\cdot[b]$
1	Mg(II)/[4] - Mn(II)/[4]	1.92	0.50	0.50	0.643
2	Mg(II)/[4] - Cr(III)/[6]	-0.76	0.50	0.67	-0.255
3	Mg(II)/[4] - Fe(III)/[6]	-0.51	0.50	0.67	-0.171
4	Mg(II)/[4] - Mn(III)/[6]	0.79	0.50	0.67	0.198
5	Mn(II)/[4] - Cr(III)/[6]	0.07	0.50	0.67	0.023
6	Mn(II)/[4] - Fe(III)/[6]	0.33	0.50	0.67	0.111
7	Mn(II)/[4] - Mn(III)/[6]	0.39	0.50	0.67	0.131
8	Cr(III)/[6] - Fe(III)/[6]	0.28	0.67	0.67	0.126
9	Cr(III)/[6] - Mn(III)/[6]	0.07	0.67	0.67	0.031
10	Fe(III)/[6] - Mn(III)/[6]	-0.19	0.67	0.67	-0.085
$\sum c_{pair}\cdot[a]\cdot[b]$					0.752
$MIntE = e^{\sum(c_{pair}\cdot[a]\cdot[b])}$					2.121

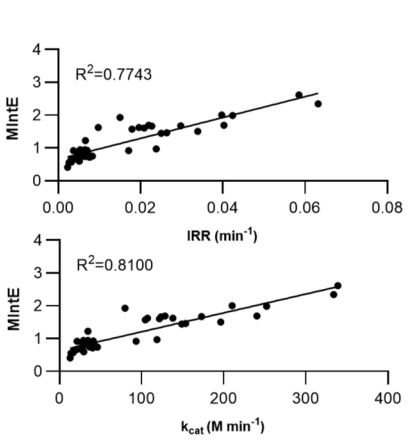

Figure 6. Structure−activity analysis of coprecipitated, single-phase MMNs. (A) GLM model description and (B) comparison of the dWAIC (±difference in standard error; dSE) values of 16 model schemes with differing information granularity. The colored dashes show the features included in each respective scheme. Lower dWAIC values indicate better model performance. (C) Coefficients of interaction terms calculated by scheme #16. Positive values (red boxes) indicate elemental combinations leading to increased k_{cat} values (synergistic interactions), while negative values (blue boxes) indicate interactions that decrease k_{cat} (antagonistic interactions). Blank white fields represent interactions that were not present in the subset of 41 materials used to train the models. (D) Equation for calculation of the mean interaction effect (MintE) value (C_{pair} = coefficient of the interaction term for a pair of ions taken from the heatmap in C) and example calculation for the material $(MgMn)(CrFeMn)_2O_4$. (E) Correlation plots of MIntE vs IRR (min^{-1}) and MintE vs k_{cat} (M min^{-1}) for the 41 single-phase materials.

https://doi.org/10.1021/acsnano.4c03053
ACS Nano 2024, 18, 19024−19037

while 41% were mixed phase and 16% appeared to be amorphous, an attribute that was not observed in the ball-milled materials. It should be noted that the crystallites of samples categorized here as amorphous may also simply be too small to be observed by XRD.

The IRR values of the top 15 performing materials were plotted, demonstrating a broad compositional variety (Figure 5A). By systematically varying the structural composition of the materials, MMNs could be prepared with 3-fold higher IRR values compared to the first subset of randomly chosen ball-milled materials (e.g., $(FeCu)(CrMnMg)_2O_4$). This observation provides compelling evidence that the large chemical space offered by MMNs can enable a further optimization of nanozyme activity. Interestingly, coprecipitated materials exhibited 10−40% lower IRR values compared to their ball-milled counterparts (Figure 5B), despite similarities in particle size (Figure S10). Within this small sample set of three materials, it was observed that material phase properties differed depending on the preparation method.

It is likely that the preparation technique itself makes a difference in terms of the reactivity, although the reasons for this remain speculative at this point. Coprecipitation allows the particles to form during a wet chemistry approach and undergo a subsequent thermal annealing step to convert the salts into oxides. The particles form slowly, and crystal growth occurs at a slower rate compared to the ball-milling process. During the calcination at several hundred degrees Celsius, the particles are given time to restructure, potentially resolving defects and gradually converting into oxides. In contrast, when ball-milling is used, materials are synthesized mechanochemically over a very short time scale. It is documented in the literature that particles prepared by ball-milling exhibit high defect densities, lattice distortions, and a broader distribution of particle sizes, including very small broken particles and larger fractions. Therefore, we postulate that differences resulting from the distinct synthesis methods will strongly affect the catalytic properties. Particularly, defect density (which significantly influences material properties) and surface structure are key factors that could make a difference and will be studied in more detail.

Computational Structure−Activity Relationship of Coprecipitated MMNs. The structure−activity relationship of the coprecipitated MMNs was explored using multiple generalized linear models (GLMs). These models build on the observation that catalysis by nanozymes follows Michaelis Menten kinetics,[5] whereby under steady-state conditions and for large substrate concentrations, $v_{max} = k_{cat}\cdot[E]_0$ (Figure 6A). k_{cat} values were employed as the dependent variable in the GLMs and were calculated by dividing the IRR (which is proportional to v_{max}) by the initial molar concentration of the material ($[E]_0$). Materials exhibiting a mixed phase (magnetite + hematite + other) were excluded from the analysis, leaving 492 IRR measurements from the 41 remaining single-phase materials for model development. Interestingly, the IRR data of the coprecipitated MMNs (Table S2) suggest that k_{cat} exhibits heteroscedasticity, i.e., its standard deviation increases with its magnitude, and the residuals around k_{cat} are skewed toward the left. To address this, the GLMs selected for further analysis used a logarithmic link function and the Gamma distribution (Figure 6A; Table S3).

Sixteen GLMs with different levels of information granularity were evaluated to model the data (Figure 6B). Model performance (i.e., best fit to the experimental data) was assessed using the widely applicable information criterion (WAIC).[63] A less negative WAIC value indicates a better performance of the model (Table S3). For easier visualization, Figure 6B shows the dWAIC values of each scheme, which result from subtracting the individual WAIC values from the least negative WAIC value of the group (scheme #16). A low dWAIC value, therefore, also represents a better model performance. Schemes ranged from simple (e.g., scheme #1 that contained only the respective molar concentrations of each element as independent variables) to more complex. Complexity and information richness were achieved by replacing the molar element concentration with molar concentrations of elements of a defined oxidation (scheme #2), coordination state (e.g., scheme #9), or both (scheme #11). Binary interactions between elements were explored by including interaction terms in the model, while the use of an indicator value for partially inverse spinel structures (PIS) was also explored. Please refer to the Supporting Information for a detailed illustration and explanation of the model schemes.

A comparison of the schemes provided interesting insights into the experimental data. For example, inclusion of the coordination state was the single most important feature to improve model performance (all eight top-performing schemes include the coordination state; #9−16). Furthermore, the four best performing schemes (#13−16) feature the coordination state combined interaction terms, indicating that specific combinations of elements in the materials could both improve or reduce catalytic activity. The top two performing model schemes (#15−16) also included information on the putative oxidation state of each element. The only difference between these two schemes was the inclusion of an indicator value for the PIS structure.

To design MMN structures with enhanced catalytic activity, it is valuable to know which combination of elements increase k_{cat}. The heatmap in Figure 6C depicts the interaction term coefficients calculated using the top-performing model (#16) and indicates which combinations increase or decrease k_{cat}. It is important to note that single elemental combinations are not representative of the overall catalytic activity since each material contains ten interaction pairs. To this end, a mean interaction effect (MIntE) value was calculated for each material (example in Figure 6D) and plotted against its corresponding IRR or k_{cat} value (Figure 6E). Both Pearson correlation (IRR: $r = 0.88$; k_{cat}: $r = 0.90$) and coefficient of determination (IRR: $R^2 = 0.77$; k_{cat}: $R^2 = 0.81$) values indicate that MIntE is a useful indicator of catalytic activity. As expected from the model, the correlation between MIntE and k_{cat} is slightly better due to the correction for the molar concentration of each element incorporated into the k_{cat} term. Importantly, it has been effectively demonstrated that GLMs can provide insight into the complex structure−activity relationship of MMNs. Furthermore, this complexity can also be elegantly summarized within a single parameter, the MIntE value, which can be employed in future work to design MMNs with higher performance.

A few limitations of the current work bear further scrutiny and offer opportunities for ongoing work to refine both the MMN production and the structure−activity models. First, it is important to note that all models developed here were based on the assumption that the elements in the 41 materials of the training set adopted the oxidation and coordination states ascribed to them in the model. However, apart from information on the molar concentrations used and the phase

https://doi.org/10.1021/acsnano.4c03053
ACS Nano 2024, 18, 19024−19037

purity from XRD patterns, the exact compositions of the coprecipitated materials are not known. Because the coprecipitation was not conducted in the absence of oxygen, it is possible that the oxidation state of materials, especially those containing multivalence cations, may differ from their assigned state. Second, despite the observation that 43% of the materials exhibited a single-phase magnetite structure, we cannot exclude the possibility that physical mixtures of different oxides all with magnetite structures are present. X-ray photoelectron spectroscopy and HR-TEM/EDS imaging are techniques that can be used to verify the oxidation state and compositional structure of MMNs, respectively, but as they are time-consuming methods, they could not be employed in this study to verify the composition of all materials tested. One strategic approach to address this in the future will be to select materials with either a high risk of oxidation during production or a poor correlation between their MIntE and IRR to investigate whether these compositions differed from the assumed states.

CONCLUSIONS

The concept of high-entropy nanomaterials inspired the design of 81 distinct MMNs containing up to six different metals, which exhibited peroxidase-like activity superior to magnetite nanozymes. The large chemical space offered by the high-entropy concept enabled the exploration of the structure–activity relationship of MMNs with a large compositional variety. The preparation of such a large library of materials was only possible through the development of a synthesis technique based on coprecipitation, instead of time-consuming preparation via ball-milling. It was observed that MMNs based on the magnetite structure ($(AA')(BB'B'')_2O_4$) but containing elemental substitutions in both the tetrahedral and octahedral sites generally exhibited a higher peroxidase-like activity compared to the materials with substitutions in the tetrahedral position only. In addition, the peroxidase-like activity of MMNs is a result of the combined effect of superoxide radicals and the electron-transfer process. Using multiple generalized linear models trained on 41 materials from the larger coprecipitated material subset, it could be inferred that catalytic activity was dependent on the total effect of all interactions between elements of a particular oxidation and coordination state. The MIntE value showed a strong correlation with catalytic activity and could be used going forward as an indicator of peroxidase-like activity when designing MMNs with superior catalytic activity for future applications, including *ex vivo* biomedical and diagnostic assay development.

EXPERIMENTAL SECTION

MMN Preparation. *Ball-Milling.* All chemicals were purchased from commercial sources (Sigma-Aldrich/Alfa-Aesar/ABCR GmbH, purity >99%) and used without further purification. For the synthesis of MMNs, the respective metal-oxide precursors (FeO, CuO, Fe_2O_3, MgO, Cr_2O_3, Mn_2O_3, and ZnO) were used in the respective molar ratios to achieve a M_3O_4 stoichiometry. The corresponding oxides were mixed and ball-milled at 500 rpm for 14–26 h in the Ar atmosphere, using a high-energy planetary ball-milling machine (Retsch PM 100, Retsch GmbH). The ball-to-powder weight ratio was 50:1. WC vials (50 mL in volume) and WC balls (5 mm in diameter) were used. Milling conditions were adjusted such that the particle size and, therefore, surface area of all materials were comparable.

Coprecipitation. The following nitrate salts were purchased from Sigma-Aldrich (purity values are given in parentheses): $Cu(NO_3)_3 \cdot 2.5H_2O$ (98%), $Cr(NO_3)_3 \cdot 9H_2O$ (99.99%), $Fe(NO_3)_3 \cdot 9H_2O$ (98%), $Mg(NO_3)_3 \cdot 6H_2O$ (99.99%), $Mn(NO_3)_3 \cdot 4H_2O$ (98%), and $Zn(NO_3)_2 \cdot 6H_2O$ (98%). The aqueous nitrate salt precursor solutions (0.2 M in distilled water) of Cu, Cr, Fe, Mg, Mn, and Zn were used for the synthesis of the respective spinel oxide compounds. In total, 70 different compositions were prepared using an automated pipetting robot (opentrons OT-2). The nitrate salt solutions were mixed in different combinations in a standard 360 μL 96-well plate. To initiate coprecipitation, the respective precursor solutions were mixed with ammonia (Sigma-Aldrich, 28–30%) at a ratio of 1:2 on a carrier substrate (two-sided polished (100) Si wafers, Macor plates), suitable for calcination and further XRD analysis. In total, 25 μL of the desired precursor solution was deposited on each of the XRD carrier substrates.

For the synthesis of larger amounts (~5 mg), the respective precursor solutions were mixed with ammonia into custom-made glass crucibles. During coprecipitation, a temperature of 70 °C was maintained. Finally, the samples were dried for approximately 1 h at 70 °C and then transferred to an oven and calcinated at 700 °C for 5 h in air. A constant heating rate of 5 °C/min and naturally cooling down to room temperature inside the oven were used.

MMN Characterization. *Automated X-ray Diffraction (XRD).* Automated XRD measurements were performed using a STOE Stadi P diffractometer equipped with a Ga-jet X-ray source (Ga–Kβ radiation, 1.2079 Å) and a custom-built XY stage for automated sample measurement. XRD patterns were obtained in transmission mode. Patterns were collected between 10 and 60° 2θ with a step size of 0.02°. The powder samples on the (100) Si wafer were fixed with a Kapton foil, and the Si wafer is held by an in-house designed holder.

MMN crystal structure, phase purity, as well as the spatial elemental distribution within the crystal were determined by transmission electron microscopy, energy-dispersive X-ray spectroscopy, and selective area electron diffraction.

Particle Size. Hydrodynamic diameters were measured with a Malvern Zetasizer ZS Nano equipped with a 633 nm laser at a scattering angle of 173° and 25 °C. Samples (10 mg) were dispersed in 10 mL of distilled water, PBS or 50 mM TRIS buffer pH 7.4 and sonicated prior to measurement. The sizes reported are mean values (±standard deviations) of number distributions of three independent dispersion experiments from a single production batch of MMNs.

Catalytic Activity. TMB is a colorless reagent, which is oxidized in the presence of H_2O_2 to colored species (λ_{max} = 650 nm). Although the reagent is oxidized by H_2O_2 alone, the reaction is accelerated by the presence of catalysts.[64,65] The reaction conditions were taken from Gao et al.[5] and further optimized (Supporting Information). Using constant substrate concentrations, the concentration of H_2O_2 was varied to achieve a measurable but low baseline reaction rate without catalyst of <0.01 min^{-1} (Figure S4A). Once the optimal H_2O_2 concentration was established, the nanozyme concentration was varied (0.4, 4, and 40 μg/mL). A minimum of 40 μg/mL nanozymes was required for reliable differentiation in catalytic activity between samples (Figure S4B). In pilot studies, it was observed that catalytically active soluble species (ions) were present in variable concentrations in the supernatant following the first dispersion in a liquid medium (Figure S4C). The presence of these catalytically active soluble species was responsible, in some cases, for masking the catalytic activity of the MMN surface. Pilot studies revealed that centrifugation, removal of the supernatant, and resuspension in fresh dispersant were sufficient to remove this source of variation. Therefore, all studies were performed with nanozymes that had been washed once prior to the assessment.

Based on the pilot studies, the following conditions were used for the TMB reactions: Nanozymes were dispersed at 80 μg/mL in either distilled water, phosphate-buffered saline (PBS), or 50 mM Tris-HCl buffer pH 7.4 and centrifuged, and the supernatant was removed and redispersed to the same concentration. Washed nanozymes (100 μL) were added to a 96-well plate and then mixed with reaction solutions to get the final reaction condition (0.2 M sodium acetate buffer pH 4)

https://doi.org/10.1021/acsnano.4c03053
ACS Nano 2024, 18, 19024–19037

in which concentrations of TMB and H_2O_2 were 800 μM and 50 mM, respectively. Dye absorption was measured every minute at 650 nm over 5 min via UV/vis spectrophotometry (EPOCH2; Biotek). The absorbance values of control wells containing sample dispersions without H_2O_2 were subtracted from each time point to account for sample absorbance. Control wells containing H_2O_2 only (no nanozymes) were measured in parallel to determine the baseline reaction rate without the catalyst. The reaction rate (min^{-1}) was calculated as the slope of the linear absorbance increase over 5 min. The increased reaction rate or IRR (min^{-1}) of the catalyst-mediated sample was calculated by subtracting the baseline reaction rate (H_2O_2 without a catalyst) from the catalyst-mediated reaction rate. IRR (min^{-1}) values presented are the mean ± standard deviation of three independent experiments with n = 4 replicates each from a single production batch. To assess batch-to-batch variability of ball-milled MMNs, a second production batch of selected materials, i.e., $(ZnCu)(FeMnCr)_2O_4$ and $(ZnCuMg)(FeMnCr)_2O_4$, was characterized (Figure S4Ei). Furthermore, stability studies with ball-milled $(Fe)Fe_2O_4$ and $(ZnCu)(FeMnCr)_2O_4$ demonstrated no significant loss in activity over 16 months of storage in the dry state at ambient room temperature (Figure S4Eii).

Hydroxyl and Superoxide Radical Assays. Hydroxyl radical detection: terephthalic acid (TA) was used as a fluorescent probe for tracking of $^{\bullet}OH$. A standard solution of sodium terephthalate (Na_2TA) with a concentration of 0.625 mM was prepared by dissolving 10.4 mg of TA in 100 mL of NaOH (1.25 mM). Around 200 μL portion of Na_2TA solution was added into a mixture of 0.2 M sodium acetate buffer pH 4 with 40 μg of MMNs and 50 mM H_2O_2. The total reaction volume was 600 μL. Then, the mixture was incubated at room temperature for 8 h, and the resulting solution was centrifuged prior to fluorescent measurement (Tecan Infinite M200). The excitation and emission wavelengths were 315 and 425 nm, respectively.

To investigate the impact of the radicals on the reaction rate, 50 μL of Na_2TA 0.625 mM or p-benzoquinone 0.1 mM (as superoxide radical scavenger) was added to the reaction mixture containing MMN and TMB/H_2O_2. Influence of radical scavengers on the reaction rate expressed as the ratio of the mean IRR without scavenger: mean IRR with scavenger (Figure 3B).

Electron-Transfer Process. About 45 μL of reduced cytochrome C solution (1 mg/mL) was added into an eppendoft, followed by the addition of 140 μL of sodium acetate buffer pH 4.0, 350 μL of MMNs dispersion (80 μg/mL), and 165 μL of distilled water. The mixture was incubated for an hour in the dark at room temperature and then centrifuged for 5 min at 13 000g. Subsequently, 200 μL of supernatant was added to a 96-well plate, and UV spectrum (Epoch2, Biotek) was scanned from 200 to 800 nm. The control sample was prepared by replacing 350 μL of the MMNs dispersion with distilled water.

Conjugation of Rabbit IgG to Nanozymes and ELISA. *Surface Modification with Antibodies.* Dispersions of selected ball-milled MMNs were prepared in PBS pH 7.4 with the addition of 0.005% polystyrene-*graft*-poly(ethylene glycol) with carboxy end groups (PS-*g*-PEG-COOH; a surfactant used for antibody conjugation to the MMN surface). Subsequently, a solution of 5% poly(ethylene glycol) (MW = 400 Da) in water (40 μL) and 1 M 2-[4-(2-hydroxyethyl)piperazin-1-yl]ethanesulfonic acid (HEPES) buffer pH 7.4 (40 μL) was added to 1 mL of MMN dispersion and mixed. A freshly prepared solution of 1% 1-ethyl-3-(3-(dimethylamino)propyl)carbodiimide in water (40 μL) and 1% 1-hydroxy-2,5-pyrrolidinedione in water (10 μL) was then added and mixed for 5 min. Rabbit IgG (367 μL of 0.1 g/L in water) was added to the mixture and stirred for 2 h at room temperature followed by the addition of 10 μL of 1% bovine serum albumin (BSA) in water. The mixture was then stirred for another 30 min. The suspensions were washed three times by centrifugation at 15 000g for 5 min and resuspended in 2 mL of PBS pH 7.4 containing 0.1% Tween 20. At the final washing step, the IgG-conjugated nanozyme dispersion was resuspended in 1 mL of PBS pH 7.4 containing 0.1% Tween 20 and 0.1% BSA. The catalytic activity of IgG-conjugated dispersions was measured as described in the Catalytic activity section.

ELISA. Preparation of the ELISA plates was performed by adding 50 μL of goat antirabbit IgG in 0.1 M borate buffer pH 9 (20 μg/mL) to a 96-well plate and incubating at 4 °C overnight. The antirabbit IgG solution was aspirated, and the wells were washed twice with 200 μL of PBS containing 0.1% Tween 20, followed by a 2 h incubation (room temperature) with 150 μL of blocking solution containing 1% BSA in PBS. Following blocking, the wells were washed twice with 200 μL of PBS containing 0.1% Tween 20. To conduct the ELISA, 100 μL IgG-conjugated nanozyme samples (concentration of 500 μg/mL in PBS pH 7.4 containing 0.1% Tween 20 and 1 mg/mL BSA) were added to each well. The plate was covered, incubated at room temperature for 2 h, and then washed three times with 200 μL of PBS containing 0.1% Tween 20 and filled with 100 μL of PBS containing 0.1% Tween 20. TMB/H_2O_2 solution (100 μL) was subsequently added to each well, and the absorbance was measured at 650 nm every minute for 5 min. Controls composed of wells containing nanozymes without the addition of H_2O_2 (for background subtraction) as well as wells containing H_2O_2 but no nanozymes (for determination of baseline reaction rate). Controls without antirabbit IgG coating were also used as a control for nonspecific binding (Figure S7). IRR (min^{-1}) values were calculated as described in the Catalytic activity section.

Computational Analysis. To ensure consistency across all samples, all IRR values were normalized by dividing the initial molar mass concentration of the corresponding composition (=k_{cat}). The relationship between composition and normalized IRR values (i.e., k_{cat}) was explored via generalized linear models using Bambi (version 0.10.0) in Python 3.[66] The package arviz (version 0.15.1)[67] was used to compute the estimated effective number of parameters, to compare models based on the WAIC and for hypothesis testing.

The MIntE was calculated by using eq 1. Each material contains 10 distinct possibilities for binary interactions, and each interaction pair was characterized by multiplying its coefficient of interaction term (shown in heatmap Figure 6C) with the individual molar concentrations of the corresponding cations with a defined oxidation and coordination state from that specific pair. The sum of these products was calculated, and the exponent of this value was equated to the MIntE. An illustration and example calculation are provided in Figure 6D.

$$\text{Mean interaction effect (MIntE)} = e^{\sum c_{pair}\cdot[a]\cdot[b]} \quad (1)$$

C_{pair}: coefficient of interaction terms
[a]: molar concentration of partner a in the interaction pair
[b]: molar concentration of partner b in the interaction pair
Please refer to the Supporting Information for illustrative examples of the models as well as further information about the MIntE value.

ASSOCIATED CONTENT

Supporting Information

The Supporting Information is available free of charge at https://pubs.acs.org/doi/10.1021/acsnano.4c03053.

Experimental procedures and characterization (DLS, HR-TEM, and XRD) of MMNs, optimization of reaction conditions for peroxidase-like activity assays, effect of prior washing/temperature/buffers on catalytic activity, batch consistency, timeline stability, steady Michaelis Menten kinetics, ELISA control experiment, and computational modeling for structure−activity relationship (PDF)

AUTHOR INFORMATION

Corresponding Authors

Ben Breitung − *Institute of Nanotechnology, Karlsruhe Institute of Technology (KIT), 76131 Karlsruhe, Germany;* orcid.org/0000-0002-1304-3398; Email: ben.breitung@kit.edu

https://doi.org/10.1021/acsnano.4c03053
ACS Nano 2024, 18, 19024−19037

Lea Ann Dailey − *Department of Pharmaceutical Sciences, University of Vienna, 1090 Vienna, Austria;* orcid.org/0000-0002-4908-7122; Email: leaann.dailey@univie.ac.at

Authors

Thuong Phan-Xuan − *Department of Pharmaceutical Sciences, University of Vienna, 1090 Vienna, Austria; Vienna Doctoral School of Pharmaceutical, Nutritional and Sport Sciences (PhaNuSpo), University of Vienna, 1090 Vienna, Austria;* orcid.org/0000-0003-4654-8699

Simon Schweidler − *Institute of Nanotechnology, Karlsruhe Institute of Technology (KIT), 76131 Karlsruhe, Germany;* orcid.org/0000-0003-4675-1072

Steffen Hirte − *Department of Pharmaceutical Sciences, University of Vienna, 1090 Vienna, Austria; Vienna Doctoral School of Pharmaceutical, Nutritional and Sport Sciences (PhaNuSpo), University of Vienna, 1090 Vienna, Austria*

Moritz Schüller − *Institute of Pharmacy, Martin-Luther-University Halle-Wittenberg, 06108 Halle, Germany*

Ling Lin − *Institute of Nanotechnology, Karlsruhe Institute of Technology (KIT), 76131 Karlsruhe, Germany*

Anurag Khandelwal − *Institute of Nanotechnology, Karlsruhe Institute of Technology (KIT), 76131 Karlsruhe, Germany; Light Technology Institute, Karlsruhe Institute of Technology, 76131 Karlsruhe, Germany*

Kai Wang − *Institute of Nanotechnology, Karlsruhe Institute of Technology (KIT), 76131 Karlsruhe, Germany; Department of Materials and Earth Sciences, Technical University Darmstadt, 64287 Darmstadt, Germany*

Jan Schütze − *Institute for Automation and Applied Informatics, Karlsruhe Institute of Technology (KIT), 76131 Karlsruhe, Germany;* orcid.org/0000-0001-5816-4866

Markus Reischl − *Institute for Automation and Applied Informatics, Karlsruhe Institute of Technology (KIT), 76131 Karlsruhe, Germany*

Christian Kübel − *Institute of Nanotechnology and Karlsruhe Nano Micro Facility (KNMFi), Karlsruhe Institute of Technology (KIT), 76131 Karlsruhe, Germany; Helmholtz Institute Ulm for Electrochemical Energy Storage, 89081 Ulm, Germany; Department of Materials and Earth Sciences, Technical University Darmstadt, 64287 Darmstadt, Germany;* orcid.org/0000-0001-5701-4006

Horst Hahn − *Institute of Nanotechnology, Karlsruhe Institute of Technology (KIT), 76131 Karlsruhe, Germany; School of Sustainable Chemical, Biological and Materials Engineering, University of Oklahoma, Norman 73019 Oklahoma, United States; Helmholtz Institute Ulm for Electrochemical Energy Storage, 89081 Ulm, Germany*

Gianluca Bello − *Department of Pharmaceutical Sciences, University of Vienna, 1090 Vienna, Austria*

Johannes Kirchmair − *Department of Pharmaceutical Sciences, University of Vienna, 1090 Vienna, Austria;* orcid.org/0000-0003-2667-5877

Jasmin Aghassi-Hagmann − *Institute of Nanotechnology, Karlsruhe Institute of Technology (KIT), 76131 Karlsruhe, Germany;* orcid.org/0000-0003-0348-041X

Torsten Brezesinski − *Institute of Nanotechnology, Karlsruhe Institute of Technology (KIT), 76131 Karlsruhe, Germany;* orcid.org/0000-0002-4336-263X

Complete contact information is available at: https://pubs.acs.org/10.1021/acsnano.4c03053

Author Contributions

††T.P.-X., S.S., and S.H. contributed equally.

Notes

The authors declare no competing financial interest.

ACKNOWLEDGMENTS

J.A.-H. acknowledges funding by the DFG under Germany's Excellence Strategy via the Excellence Cluster "3D Matter Made to Order" (EXC-2082/1-390761711). H.H. acknowledges the financial support by the Deutsche Forschungsgemeinschaft under contract HA 1344/45-1. K.W. and L.L. acknowledge financial support by the Chinese Scholarship Council (CSC). T.P.-X. acknowledges financial support from the Ernst Mach scholarship ASEA-UNINET funded by the Austrian Federal Ministry of Education, Science and Research (BMBWF), and the PhaNuSpo Completion scholarship sponsored by Vienna Doctoral School of Pharmaceutical, Nutritional and Sport Sciences, University of Vienna. The authors acknowledge George Mathew for artwork preparation. S.S., J.A.-H., and B.B. acknowledge financial support from the KIT via the project Auto.MAP and the Helmholtz Program "Materials Systems Engineering" under program no. 43.31.01.

REFERENCES

(1) Zhang, R.; Fan, K.; Yan, X. Nanozymes: Created by Learning from Nature. *Sci. China: Life Sci.* **2020**, *63* (8), 1183−1200.

(2) Wei, H.; Wang, E. Nanomaterials with Enzyme-like Characteristics (Nanozymes): Next-Generation Artificial Enzymes. *Chem. Soc. Rev.* **2013**, *42* (14), 6060−6093.

(3) Zhang, J.; Liu, J. Light-Activated Nanozymes: Catalytic Mechanisms and Applications. *Nanoscale* **2020**, *12*, 2914−2923, DOI: 10.1039/c9nr10822j.

(4) Liu, E.; Wu, J.; Liang, T.; Zhang, B.; Tang, Z.; Qu, S. Toward Rational Design of Carbon Nanodots with High Photothermal Efficiency for Tumor Photothermal Therapy†. *Chin. J. Chem.* **2023**, *41* (16), 1994−2001.

(5) Gao, L.; Zhuang, J.; Nie, L.; Zhang, J.; Zhang, Y.; Gu, N.; Wang, T.; Feng, J.; Yang, D.; Perrett, S.; Yan, X. Intrinsic Peroxidase-like Activity of Ferromagnetic Nanoparticles. *Nat. Nanotechnol* **2007**, *2* (9), 577−583.

(6) Rodríguez-López, J. N.; Lowe, D. J.; Hernández-Ruiz, J.; Hiner, A. N. P.; García-Cánovas, F.; Thorneley, R. N. F. Mechanism of Reaction of Hydrogen Peroxide with Horseradish Peroxidase: Identification of Intermediates in the Catalytic Cycle. *J. Am. Chem. Soc.* **2001**, *123*, 11838−11847.

(7) Moreno Maldonado, A. C.; Winkler, E. L.; Raineri, M.; Córdova, A. T.; Rodríguez, L. M.; Troiani, H. E.; Pisciotti, M. L. M.; Mansilla, M. V.; Tobia, D.; Nadal, M. S.; Torres, T. E.; De Biasi, E.; Ramos, C. A.; Goya, G. F.; Zysler, R. D.; Lima, E. Free-Radical Formation by the Peroxidase-Like Catalytic Activity of MFe2O4 (M = Fe, Ni, and Mn) Nanoparticles. *J. Phys. Chem. C* **2019**, *123* (33), 20617−20627.

(8) Meunier, B.; Robert, A. Comment on "Free-Radical Formation by the Peroxidase-Like Catalytic Activity of MFe2O4 (M = Fe, Ni, and Mn) Nanoparticles. *J. Phys. Chem. C* **2019**, *123* (46), 28513−28514.

(9) Moreno Maldonado, A. C.; L Winkler, E.; Raineri, M.; Toro Córdova, A.; M Rodríguez, L.; E Troiani, H.; Luz Mojica Pisciotti, M.; Vasquez Mansilla, M.; Tobia, D.; S Nadal, M.; E Torres, T.; De Biasi, E.; A Ramos, C.; F Goya, G.; D Zysler, R.; Lima, E., Jr. Reply to "Comment on 'Free-Radical Formation by the Peroxidase-Like Catalytic Activity of MFe2O4 (M = Fe, Ni, and Mn) Nanoparticles'". *J. Phys. Chem. C* **2019**, *123* (46), 28511−28512.

(10) Liu, M.; Ye, Y.; Ye, J.; Gao, T.; Wang, D.; Chen, G.; Song, Z. Recent Advances of Magnetite (Fe3O4)-Based Magnetic Materials in Catalytic Applications. *Magnetochemistry* **2023**, *9* (4). 110.

(11) Gao, L.; Fan, K.; Yan, X. Iron Oxide Nanozyme: A Multifunctional Enzyme Mimetic for Biomedical Applications. *Theranostics* **2017**, *7* (13), 3207−3227.
(12) Lu, C.; Zandieh, M.; Zheng, J.; Liu, J. Comparison of the Peroxidase Activities of Iron Oxide Nanozyme with DNAzyme and Horseradish Peroxidase. *Nanoscale* **2023**, *15* (18), 8189−8196.
(13) Fan, K.; Wang, H.; Xi, J.; Liu, Q.; Meng, X.; Duan, D.; Gao, L.; Yan, X. Optimization of Fe3O4 Nanozyme Activity via Single Amino Acid Modification Mimicking an Enzyme Active Site. *Chem. Commun.* **2017**, *53* (2), 424−427.
(14) Sun, X.; Guo, S.; Chung, C. S.; Zhu, W.; Sun, S. A Sensitive H2O2 Assay Based on Dumbbell-like PtPd-Fe3O4 Nanoparticles. *Adv. Mater.* **2013**, *25* (1), 132−136.
(15) Jiang, Y.; Ding, Z.; Gao, M.; Chen, C.; Ni, P.; Zhang, C.; Wang, B.; Duan, G.; Lu, Y. Spontaneous Deposition of Uniformly Distributed Ruthenium Nanoparticles on Graphitic Carbon Nitride for Quantifying Electrochemically Accumulated H2O2. *Chin. J. Chem.* **2021**, *39* (12), 3369−3374.
(16) Huang, L.; Chen, J.; Gan, L.; Wang, J.; Dong, S. Single-Atom Nanozymes. *Sci. Adv.* **2019**, *5* (5), No. eaav5490, DOI: 10.1126/sciadv.aav5490.
(17) Jiang, B.; Liang, M. Advances in Single-Atom Nanozymes Research†. *Chin. J. Chem.* **2021**, *39* (1), 174−180.
(18) Liu, B.; Liu, J. Accelerating Peroxidase Mimicking Nanozymes Using DNA. *Nanoscale* **2015**, *7* (33), 13831−13835.
(19) Shi, W.; Zhang, X.; He, S.; Huang, Y. CoFe2O4Magnetic Nanoparticles as a Peroxidase Mimic Mediated Chemiluminescence for Hydrogen Peroxide and Glucose. *Chem. Commun.* **2011**, *47* (38), 10785−10787.
(20) Su, L.; Qin, W.; Zhang, H.; Rahman, Z. U.; Ren, C.; Ma, S.; Chen, X. The Peroxidase/Catalase-like Activities of MFe2O4 (M = Mg, Ni, Cu) MNPs and Their Application in Colorimetric Biosensing of Glucose. *Biosens. Bioelectron.* **2015**, *63*, 384−391.
(21) Luo, L.; Zhang, Y.; Li, F.; Si, X.; Ding, Y.; Deng, D.; Wang, T. Enzyme Mimics of Spinel-Type CoxNi1-XFe2O4Magnetic Nanomaterial for Eletroctrocatalytic Oxidation of Hydrogen Peroxide. *Anal. Chim. Acta* **2013**, *788*, 46−51.
(22) Rost, C. M.; Sachet, E.; Borman, T.; Moballegh, A.; Dickey, E. C.; Hou, D.; Jones, J. L.; Curtarolo, S.; Maria, J. P. Entropy-Stabilized Oxides. *Nat. Commun.* **2015**, *6*, No. 8485, DOI: 10.1038/ncomms9485.
(23) Sarkar, A.; Breitung, B.; Hahn, H. High Entropy Oxides: The Role of Entropy, Enthalpy and Synergy. *Scr Mater.* **2020**, *187*, 43−48.
(24) Akrami, S.; Edalati, P.; Fuji, M.; Edalati, K. High-Entropy Ceramics: Review of Principles, Production and Applications. *Materials Science and Engineering R: Reports* **2021**, *146*. 100644.
(25) Gludovatz, B.; Hohenwarter, A.; Catoor, D.; Chang, E. H.; George, E. P.; Ritchie, R. O. A Fracture-Resistant High-Entropy Alloy for Cryogenic Applications. *Science* **2014**, *345* (6201), 1153−1158.
(26) Chikumba, S.; Rao, V. V. High Entropy Alloys: Development and Applications. In *7th International Conference on Latest Trends in Engineering and Technology (ICLTET'2015) Nov.26−27.2015 Irene Pretoria (South Africa) 1−5*; International Institute of Engineers, 2015. DOI: 10.15242/iie.e1115005.
(27) Vasilievna, O.; Leticia, K.; Torres-Martínez, M.; Kharisov, B. I. *Handbook of Nanomaterials and Nanocomposites for Energy and Environmental Applications*; Springer: Cham, 2021; Vol. 3, pp 1899−2747 DOI: 10.1007/978-3-030-36268-3.
(28) Deng, Z.; Olvera, A.; Casamento, J.; Lopez, J. S.; Williams, L.; Lu, R.; Shi, G.; Poudeu, P. F. P.; Kioupakis, E. Semiconducting High-Entropy Chalcogenide Alloys with Ambi-Ionic Entropy Stabilization and Ambipolar Doping. *Chem. Mater.* **2020**, *32* (14), 6070−6077.
(29) Schweidler, S.; Botros, M.; Strauss, F.; Wang, Q.; Ma, Y.; Velasco, L.; Cadilha Marques, G.; Sarkar, A.; Kübel, C.; Hahn, H.; Aghassi-Hagmann, J.; Brezesinski, T.; Breitung, B. High-Entropy Materials for Energy and Electronic Applications. *Nat. Rev. Mater.* **2024**, *9*, 266.
(30) Wang, K.; Hua, W.; Huang, X.; Stenzel, D.; Wang, J.; Ding, Z.; Cui, Y.; Wang, Q.; Ehrenberg, H.; Breitung, B.; Kübel, C.; Mu, X. Synergy of Cations in High Entropy Oxide Lithium Ion Battery Anode. *Nat. Commun.* **2023**, *14* (1), No. 1487, DOI: 10.1038/s41467-023-37034-6.
(31) Sarkar, A.; Velasco, L.; Wang, D.; Wang, Q.; Talasila, G.; de Biasi, L.; Kübel, C.; Brezesinski, T.; Bhattacharya, S. S.; Hahn, H.; Breitung, B. High Entropy Oxides for Reversible Energy Storage. *Nat. Commun.* **2018**, *9* (1), No. 3400, DOI: 10.1038/s41467-018-05774-5.
(32) Li, S.; Tang, X.; Jia, H.; Li, H.; Xie, G.; Liu, X.; Lin, X.; Qiu, H. J. Nanoporous High-Entropy Alloys with Low Pt Loadings for High-Performance Electrochemical Oxygen Reduction. *J. Catal.* **2020**, *383*, 164−171.
(33) Huang, K.; Zhang, B.; Wu, J.; Zhang, T.; Peng, D.; Cao, X.; Zhang, Z.; Li, Z.; Huang, Y. Exploring the Impact of Atomic Lattice Deformation on Oxygen Evolution Reactions Based on a Sub-5 Nm Pure Face-Centred Cubic High-Entropy Alloy Electrocatalyst. *J. Mater. Chem. A* **2020**, *8* (24), 11938−11947.
(34) Jia, Z.; Yang, T.; Sun, L.; Zhao, Y.; Li, W.; Luan, J.; Lyu, F.; Zhang, L. C.; Kruzic, J. J.; Kai, J. J.; Huang, J. C.; Lu, J.; Liu, C. T. A Novel Multinary Intermetallic as an Active Electrocatalyst for Hydrogen Evolution. *Adv. Mater.* **2020**, *32* (21), No. 2000385, DOI: 10.1002/adma.202000385.
(35) Nellaiappan, S.; Katiyar, N. K.; Kumar, R.; Parui, A.; Malviya, K. D.; Pradeep, K. G.; Singh, A. K.; Sharma, S.; Tiwary, C. S.; Biswas, K. High-Entropy Alloys as Catalysts for the CO2 and CO Reduction Reactions: Experimental Realization. *ACS Catal.* **2020**, *10* (6), 3658−3663.
(36) Ai, Y.; He, M. Q.; Sun, H.; Jia, X.; Wu, L.; Zhang, X.; Sun, H. bin.; Liang, Q. Ultra-Small High-Entropy Alloy Nanoparticles: Efficient Nanozyme for Enhancing Tumor Photothermal Therapy. *Adv. Mater.* **2023**, *35*, No. 2302335.
(37) Rashidy Ahmady, A.; Ekhlasi, A.; Nouri, A.; Haghbin Nazarpak, M.; Gong, P.; Solouk, A. High Entropy Alloy Coatings for Biomedical Applications: A Review. *Smart Mater. Manuf.* **2023**, *1*, No. 100009.
(38) Feng, J.; Yang, X.; Du, T.; Zhang, L.; Zhang, P.; Zhuo, J.; Luo, L.; Sun, H.; Han, Y.; Liu, L.; Shen, Y.; Wang, J.; Zhang, W. Transition Metal High-Entropy Nanozyme: Multi-Site Orbital Coupling Modulated High-Efficiency Peroxidase Mimics. *Adv. Sci.* **2023**, *10* (33), No. e2303078, DOI: 10.1002/advs.202303078.
(39) Xie, M.; Fang, W.; Qu, Z.; Hu, Y.; Zhang, Y.; Chao, J.; Shi, J.; Wang, L.; Wang, L.; Tian, Y.; Fan, C.; Liu, H. High-Entropy Alloy Nanopatterns by Prescribed Metallization of DNA Origami Templates. *Nat. Commun.* **2023**, *14* (1), No. 1745, DOI: 10.1038/s41467-023-37333-y.
(40) Shannon, R. D. Revised Effective Ionic Radii and Systematic Studies of Interatomic Distances in Halides and Chalcogenides. *Acta Crystallogr.* **1976**, *A32*, 751−767.
(41) Sun; Dai, Y. High-Entropy Materials for Catalysis: A New Frontier. *Sci. Adv.* **2021**, *7* (20), No. eabg1600.
(42) Li, M.; Liu, J.; Xu, Y.; Qian, G. Phosphate Adsorption on Metal Oxides and Metal Hydroxides: A Comparative Review. *Environ. Rev.* **2016**, *24* (3), 319−332.
(43) Muthukumaran, T.; Philip, J. Effect of Phosphate and Oleic Acid Capping on Structure, Magnetic Properties and Thermal Stability of Iron Oxide Nanoparticles. *J. Alloys Compd.* **2016**, *689*, 959−968.
(44) Ng, Y. H.; Chin, S. F.; Pang, S. C.; Ng, S. M. Utilising the Interface Interaction on Tris(Hydroxymethy)Aminomethane-Capped Carbon Dots to Enhance the Sensitivity and Selectivity towards the Detection of Co(II) Ions. *Sens. Actuators, B* **2018**, *273*, 83−92.
(45) Zhang, R.; Zhao, H.; Fan, K.Structure-Activity Mechanism of Iron Oxide Nanozymes. In *Nanozymes: Design, Synthesis, and Applications*, ACS Symposium Series; American Chemical Society, 2022; Vol. *1422*, pp 1−35. DOI: 10.1021/bk-2022-1422.ch001.
(46) Costa, R. C. C.; Lelis, M. F. F.; Oliveira, L. C. A.; Fabris, J. D.; Ardisson, J. D.; Rios, R. R. V. A.; Silva, C. N.; Lago, R. M. Novel Active Heterogeneous Fenton System Based on Fe3-XM XO4 (Fe, Co, Mn, Ni): The Role of M2+ Species on the Reactivity towards H2O2 Reactions. *J. Hazard. Mater.* **2006**, *129* (1−3), 171−178.

(47) Liang, X.; He, Z.; Wei, G.; Liu, P.; Zhong, Y.; Tan, W.; Du, P.; Zhu, J.; He, H.; Zhang, J. The Distinct Effects of Mn Substitution on the Reactivity of Magnetite in Heterogeneous Fenton Reaction and Pb(II) Adsorption. *J. Colloid Interface Sci.* **2014**, *426*, 181−189.
(48) Ramankutty, C. G.; Sugunan, S.; Thomas, B. Study of Cyclohexanol Decomposition Reaction over the Ferrospinels, A1−xCuxFe2O4 (A = Ni or Co and X = 0, 0.3, 0.5, 0.7 and 1), Prepared by 'Soft' Chemical Methods. *J. Mol. Catal. A: Chem.* **2002**, *187* (1), 105−117.
(49) Xia, F.; Shi, Q.; Nan, Z. Facile Synthesis of Cu-CuFe2O4nanozymes for Sensitive Assay of H2O2and GSH. *Dalton Trans.* **2020**, *49* (36), 12780−12792.
(50) Wu, L.; Wan, G.; Hu, N.; He, Z.; Shi, S.; Suo, Y.; Wang, K.; Xu, X.; Tang, Y.; Wang, G. Synthesis of Porous CoFe2O4 and Its Application as a Peroxidase Mimetic for Colorimetric Detection of H2O2 and Organic Pollutant Degradation. *Nanomaterials* **2018**, *8* (7). 451.
(51) Su, L.; Feng, J.; Zhou, X.; Ren, C.; Li, H.; Chen, X. Colorimetric Detection of Urine Glucose Based ZnFe2O4Magnetic Nanoparticles. *Anal. Chem.* **2012**, *84* (13), 5753−5758.
(52) Yu, F.; Huang, Y.; Cole, A. J.; Yang, V. C. The Artificial Peroxidase Activity of Magnetic Iron Oxide Nanoparticles and Its Application to Glucose Detection. *Biomaterials* **2009**, *30* (27), 4716−4722.
(53) Jiang, B.; Duan, D.; Gao, L.; Zhou, M.; Fan, K.; Tang, Y.; Xi, J.; Bi, Y.; Tong, Z.; Gao, G. F.; Xie, N.; Tang, A.; Nie, G.; Liang, M.; Yan, X. Standardized Assays for Determining the Catalytic Activity and Kinetics of Peroxidase-like Nanozymes. *Nat. Protoc.* **2018**, *13* (7), 1506−1520.
(54) Cai, R.; Yang, D.; Yan, L.; Tian, F.; Zhang, J.; Lyu, Y.; Chen, K.; Hong, C.; Chen, X.; Zhao, Y.; Chen, Z.; Tan, W. Free-Floating 2D Nanosheets with a Superlattice Assembled from Fe3O4 Nanoparticles for Peroxidase-Mimicking Activity. *ACS Appl. Nano Mater.* **2018**, *1* (10), 5389−5395.
(55) Song, C.; Ding, W.; Zhao, W.; Liu, H.; Wang, J.; Yao, Y.; Yao, C. High Peroxidase-like Activity Realized by Facile Synthesis of FeS2 Nanoparticles for Sensitive Colorimetric Detection of H2O2 and Glutathione. *Biosens. Bioelectron.* **2020**, *151*. 111983.
(56) Wang, C.; Gao, J.; Cao, Y.; Tan, H. Colorimetric Logic Gate for Alkaline Phosphatase Based on Copper (II)-Based Metal-Organic Frameworks with Peroxidase-like Activity. *Anal. Chim. Acta* **2018**, *1004*, 74−81.
(57) Liang, L.; Zhao, Z.; Ye, F.; Zhao, S. Rapid and Sensitive Colorimetric Detection of Dopamine Based on the Enhanced-Oxidase Mimicking Activity of Cerium(Iv). *New J. Chem.* **2021**, *45* (15), 6780−6786.
(58) Warkhade, S. K.; Singh, R. P.; Das, R. S.; Gaikwad, G. S.; Zodape, S. P.; Pratap, U. R.; Maldhure, A.; Wankhade, A. V. CoSe2 Nanoflakes: An Artificial Nanoenzyme with Excellent Peroxidase like Activity. *Inorg. Chem. Commun.* **2021**, *126*. 108461.
(59) Chen, T. M.; Wu, X. J.; Wang, J. X.; Yang, G. W. WSe2 Few Layers with Enzyme Mimic Activity for High-Sensitive and High-Selective Visual Detection of Glucose. *Nanoscale* **2017**, *9* (32), 11806−11813.
(60) Yin, D.; Yang, H.; Wang, S.; Yang, Z.; Liu, Q.; Zhang, X.; Zhang, X. Ce-Doped ZnCo2O4 Nanospheres: Synthesis, Double Enzyme-like Performances, Catalytic Mechanism and Fast Colorimetric Determination for Glutathione. *Colloids Surf., A* **2020**, *607*. 125466.
(61) Zhou, L.; Liu, Y.; Lu, Y.; Zhou, P.; Lu, L.; Lv, H.; Hai, X. Recent Advances in the Immunoassays Based on Nanozymes. *Biosensors* **2022**, *12* (12), 1119 DOI: 10.3390/bios12121119.
(62) Raineri, M.; Winkler, E. L.; Torres, T. E.; Vasquez Mansilla, M.; Nadal, M. S.; Zysler, R. D.; Lima, E. Effects of Biological Buffer Solutions on the Peroxidase-like Catalytic Activity of Fe3O4 Nanoparticles. *Nanoscale* **2019**, *11* (39), 18393−18406.
(63) Vehtari, A.; Gelman, A.; Gabry, J. Practical Bayesian Model Evaluation Using Leave-One-out Cross-Validation and WAIC. *Stat. Comput.* **2017**, *27* (5), 1413−1432.
(64) Josephy, P. D.; Eling, T.; Mason, R. P. The Horseradish Peroxidase-Catalyzed Oxidation of 3,5,3′,5′-Tetramethylbenzidine. Free Radical and Charge-Transfer Complex Intermediates. *J. Biol. Chem.* **1982**, *257* (7), 3669−3675.
(65) Zhang, S.; Yang, J.; Lin, J. 3,3′-Diaminobenzidine (DAB)-H2O2-HRP Voltammetric Enzyme-Linked Immunoassay for the Detection of Carcionembryonic Antigen. *Bioelectrochemistry* **2008**, *72* (1), 47−52.
(66) Capretto, T.; Piho, C.; Kumar, R.; Westfall, J.; Yarkoni, T.; Martin, O. A. Bambi: A Simple Interface for Fitting Bayesian Linear Models in Python. *J. Stat. Software* **2022**, *103* (15), 1−29, DOI: 10.18637/jss.v103.i15.
(67) Kumar, R.; Carroll, C.; Hartikainen, A.; Martin, O. ArviZ a Unified Library for Exploratory Analysis of Bayesian Models in Python. *J. Open Source Software* **2019**, *4* (33), 1143.